

Analysis of structures in the cross sections for elastic scattering and spin exchange in low-energy $H^+ + H$ collisions

P. S. Krstić,¹ J. H. Macek,² S. Yu. Ovchinnikov,² and D. R. Schultz¹

¹*Physics Division, Oak Ridge National Laboratory, Oak Ridge, Tennessee 37831, USA*

²*Department of Physics and Astronomy, University of Tennessee, Knoxville, Tennessee 37996-1501, USA*

(Received 20 April 2004; published 18 October 2004)

Elastic scattering and spin exchange cross sections in $H^+ + H$ collisions are computed using accurate adiabatic potential curves for the center-of-mass energy range $10^{-4} < E < 100$ eV. Both cross sections show considerable structure which necessitates computation on a fine energy grid to resolve them. We analyze the structures using a comparison equation method to find the poles of the scattering matrix in the complex energy plane. We show that many features of the cross sections can be correlated with these poles and tabulate the positions of the most important poles. Finding stationary phases in the partial wave cross sections, we also explain in all details the glory oscillations of the elastic cross section that extends below 100 eV down to the lowest energies.

DOI: 10.1103/PhysRevA.70.042711

PACS number(s): 34.50.-s, 52.20.Hv

I. INTRODUCTION

The elastic scattering and spin exchange cross sections for proton impact on atomic hydrogen are important for applications such as the study of fusion and astrophysical plasmas. For that reason, calculations have been published over the years which usually employ the most accurate techniques available at the time [1–6]. In the low-energy range, that is for impact energies below the first excitation threshold near 10 eV, the cross sections show considerable structure which makes a detailed physical analysis of the underlying comparison of different calculations problematical unless the energy grid is extremely fine and the results computed with great accuracy. Previous calculations have tended toward this direction, but still greater accuracy is needed. In this manuscript we report more accurate calculations on a fine energy grid for center-of-mass collision energies $E < 100$ eV. These calculations are described in Sec. II A.

It is a particular goal to interpret the source of the structures seen in the computed cross sections given that some structure is predicted for all ion-atom collisions in this energy range [7]. The $H^+ + H$ system is an ideal prototype to study the origins of these ubiquitous structures. For that reason we exploit the present high-energy-resolution calculations to identify generic features that may be present in most ion-atom collisions at sufficiently low energy.

It is known that structures in cross sections are often related to analytic properties of the underlying scattering matrix elements in the complex energy plane. In the case of narrow, isolated resonances, it is also possible to use the Fano line-shape theory [8] or the standard Breit-Wigner resonance theory [9] to characterize the structure. Hodges and Breig [3] identified some of the narrow features that showed a Lorentzian line shape with shape resonances corresponding to waves trapped in a combination of an attractive potential and an angular momentum barrier. In the present case, use of these standard theories for all structures is not appropriate owing to the large apparent width of some of the features.

A better strategy is to relate structures to unique quantities, namely, the values of complex energies where the S

matrix has poles. Unfortunately, computing hundreds of partial waves for complex values of E presents formidable numerical difficulties. Fortunately, accurate approximate formulas [10] based upon the comparison equation method are available that allow analytic continuation into the complex energy plane so that positions of resonance poles can be computed more tractably. In the work reported here, the positions and widths are calculated and correlated with the structures seen in the cross sections. These identifications are described in Sec. II B.

Not all of the resonances show up in the total cross section. This happens because several poles correspond to window resonances that are best seen in the partial cross sections for a given angular momentum. For that reason a selection of partial waves is examined in more detail. The narrow resonances are shown to fit the Fano line-shape formula, while the broadest resonances do not. This analysis is presented in Sec. II C.

Additional features beyond those related to resonances are seen in the elastic scattering cross section, but not in the spin exchange cross section. One of the most conspicuous of these features is a regular oscillation above energies of the order of 2 eV. This feature is analyzed in Sec. II C in terms of the glory mechanism (see Refs. [11,12]). Our concluding remarks are given in Sec. III.

Atomic system of units will be used throughout the text, unless otherwise stated.

II. CALCULATION, RESULTS, AND DISCUSSION

A. Cross-section calculation

The radial wave functions which define the $H^+ + H$ scattering amplitudes satisfy Schrödinger equations in uncoupled partial waves of angular momenta L , and for most of the energy range considered (10^{-4} –10 eV) these are simple, state-uncoupled second-order ordinary differential equations of the form (see, for example, Refs. [4–6] and references therein)

$$\left[\frac{d^2}{dR^2} - \frac{L(L+1)}{R^2} - 2\mu E_a(R) + 2\mu E \right] F_a^{(L)}(R) = 0, \quad (1)$$

where $E_a(R)$ is an adiabatic electronic potential as a function of internuclear distance R for either the $1s\sigma_g$ or $2p\sigma_u$ state of $H^+ + H$, μ is the system reduced mass, and $F_a^{(L)}(R)$ is the nuclear wave function of the channel a . Of course, each of the gerade states may, in fact, be coupled with the excited gerade states. These are here below the threshold for the reaction, since the $H(n=2)$ state is 10.2 eV above the ground, $H(n=1)$, state. Inelastic transition to $H(n=2)$, through Coriolis coupling of the $2p\sigma$ and $2p\pi$ molecular states, becomes important above about $E=50$ eV, contributing up to 2% to the elastic and momentum-transfer cross sections. This transition is taken into account in our calculation, as described earlier [4].

Elastic scattering takes place in each of the channels $1s\sigma_g$ or $2p\sigma_u$ and the total channel wave function has the asymptotic form

$$F_a(\vec{R})|_{R \rightarrow \infty} \rightarrow \exp(i\vec{k} \cdot \vec{R}) + f_a(\theta) \frac{\exp(ikR)}{R}, \quad (2)$$

where $f_a(\theta)$ are the scattering amplitudes for the scattering angle θ , written in terms of the S -matrix elements as

$$f(\theta) = \frac{1}{2ik} \sum_{L=0}^{\infty} (2L+1)(S_L-1)P_L(\cos \theta), \quad (3)$$

where S_L can be expressed in terms of the phase shifts η_L , $S_L = \exp(i2\eta_L)$ and k is the wave vector related to the center-of-mass velocity. The phase shifts for each partial wave were calculated as

$$\eta_L^a = \text{mod} \left(\frac{1}{2} \arctan \left(\frac{\text{Im}\{S_L^a\}}{\text{Re}\{S_L^a\}} \right), 2\pi \right), \quad (4)$$

where S_L^a are the S -matrix elements for the channel a , calculated as $S_L^a = F_a^{(L)}(R \rightarrow \infty)$.

A considerable confusion in applications of elastic scattering data may arise due to the difference between the classical and quantum-mechanical definitions of elastic scattering and charge transfer for slow collisions involving identical nuclei such as is in $H^+ + H$. The indistinguishability of identical particles results in the inability to differentiate slow protons elastically scattered by H from the recoiling target protons produced by charge transfer. This phenomenon is manifested through interference of the wave functions for the elastic and charge transfer channels. At higher collision energies the overlap of the two channels vanishes, leading to pronounced peaks in the differential cross sections for forward (elastic) and backward (charge transfer) scattering. Thus the elastic cross section defined quantum mechanically tends, at higher collision energies, to the total scattering cross section (i.e., the sum of classically distinguishable elastic scattering and charge transfer). At these higher energies one could calculate or measure the elastic cross section for scattering of the projectile separately from charge transfer or target recoil. We have shown that this limit is reached for $E > 1$ eV. However, to maintain a quantum-mechanically

correct definition, consistent with conventions well established in the literature [3,13] in the energy range considered here, we treat the identical nuclei as indistinguishable, even for $E > 1$ eV, when the “elastic” cross-section transitions to the total scattering cross section, containing the nonoverlapping sum of direct and recoil channels.

In general, if the nuclei are identical and the collision energy is low enough, there is no way to distinguish which ion is elastically scattered and which ion results from charge transfer from the target nuclei, unless we label the particles by their spin. Thus our use of the term spin exchange to describe charge transfer in this system. In a typical situation of an unpolarized projectile beam and target we must account for the appropriate spin statistics, which yields elastic cross sections that contain contributions from both channels coherently. With the increase of collision energy these evolve into the “total” scattering cross sections for the projectiles.

This may be formalized by first defining the relative center-of-mass motion of the nuclei by the vector $\vec{R} = \vec{R}_1 - \vec{R}_2$. The interchange of particles results in the change of the sign $\vec{R} \rightarrow -\vec{R}$, or equivalently, the change of scattering angle θ into $\pi - \theta$ while \vec{R} is unchanged. A detector at angle θ would count both particles scattered at θ and $\pi - \theta$. When nuclei have the same charge but are distinguishable by other means, the scattering amplitude for the direct elastic $f_d(\theta)$ and charge transfer $f_{ct}(\theta)$ channels are commonly defined in terms of scattering amplitudes on uncoupled gerade and ungerade ground states [14,15], i.e.,

$$f_d(\theta) = \frac{f_g(\theta) + f_u(\theta)}{2} \quad (5)$$

and

$$f_{ct}(\theta) = \frac{f_g(\theta) - f_u(\theta)}{2}. \quad (6)$$

In the fully nuclear-symmetric case considered here, taking into account spin statistics of an unpolarized beam on an unpolarized target, one obtains [13–15]

$$\frac{d\sigma_{\text{tot}}}{d\Omega} = s_1 |f_d(\theta) - f_{ct}(\pi - \theta)|^2 + s_2 |f_d(\theta) + f_{ct}(\pi - \theta)|^2, \quad (7)$$

where $s_1 = \frac{3}{4}$ and $s_2 = \frac{1}{4}$. We use subscript “tot” for the cross section in Eq. (7), rather than the usual “el,” thus stressing the true meaning of the equation in the classically distinguishable particle (CDP) limit, at higher energies, i.e., an incoherent combination of elastic scattering and charge transfer.

Thus for the present symmetric (sym) $H^+ + H$ system with fermion nuclei, performing integration over scattering angles analytically, the formulas obtained for the integral elastic cross section take the form

$$\sigma_{\text{tot, sym}} = \frac{4\pi}{k^2} \sum_{L=\pm} (2L+1) (\omega_g^+ \sin^2 \eta_l^g + \omega_u^+ \sin^2 \eta_l^u), \quad (8)$$

where the coefficients ω_l^\pm for even (+) and odd (−) L are defined as $\omega_g^+ = 1/4$, $\omega_u^+ = 3/4$, and $\omega_g^- = 3/4$, $\omega_u^- = 1/4$, respectively.

If the incident flux of protons is polarized (for example of spin $1/2$), and we are able to measure the spin of the protons reaching the detector, the protons of spin $-1/2$ originated in the unpolarized hydrogen target. Thus one defines the cross section for charge transfer involving protons and hydrogen atoms of different nuclear spins, i.e., spin exchange. In this way we are able to distinguish the nuclei of the projectile and of the target by their spin assuming a polarized incident beam; one defines the amplitude for spin exchange [13,15] as $f_{\text{se}}(\theta) = f_{\text{ct}}(\theta)$, Eq. (6). The spin exchange obviously acquires the meaning of the charge transfer amplitude when CDP is applicable; therefore from here forward we will use the subscript “ct” for either charge transfer or spin exchange. The spin exchange cross section is defined by [13–15]

$$\frac{d\sigma_{\text{ct}}}{d\Omega} = \frac{1}{4} |f_g(\pi - \theta) - f_u(\pi - \theta)|^2 \equiv |f_{\text{ex}}(\pi - \theta)|^2, \quad (9)$$

where the dependence on $\pi - \theta$ comes from the fact that the detected flux is that of the recoiled target protons. Substituting in the given amplitudes we find

$$\frac{d\sigma_{\text{ct}}}{d\Omega} = \frac{1}{k^2} \left| \sum_{L=0}^{\infty} (2L+1) \exp[i(\eta_l^g + \eta_l^u)] \sin(\eta_l^g - \eta_l^u) P_L(\cos \theta) \right|^2 \quad (10)$$

which yields

$$\sigma_{\text{ct, sym}} = \frac{4\pi}{k^2} \sum_{L=0}^{\infty} (2L+1) \sin^2(\eta_l^g - \eta_l^u). \quad (11)$$

It is interesting to consider the behavior of these cross sections at relatively high collision energies where $f_{g,u}(\theta)$ are sharply peaked in a narrow cone about $\theta=0$. As a consequence, the overlap of $f_{g,u}(\theta)$ and $f_{g,u}(\pi - \theta)$ is minimal for small θ and they do not interfere. Then Eq. (7) can be written in the classical limit as

$$\frac{d\sigma_{\text{el}}}{d\Omega} \approx |f_d(\theta)|^2 + |f_{\text{ex}}(\pi - \theta)|^2 \quad (12)$$

which is the total differential cross section for detecting protons at an angle θ both by scattering of the beam of protons on the target of H atoms and by capturing electrons from the target atoms, assuming we have means of distinguishing the scattered and charge-transfer fluxes (for example by spin, or by energy). In that case, the charge-transfer flux is in a small cone around $\theta=\pi$, while the elastic flux is peaked around $\theta=0$.

Furthermore, in this classical limit, one can define separately “pure” elastic ($\propto |f_d(\theta)|^2$) and charge transfer ($\propto |f_{\text{ct}}(\theta)|^2$) cross sections. The latter represents the flux of H

atoms formed through electron capture to the impacting beam of protons. The corresponding flux of protons $|f_{\text{ct}}(\pi - \theta)|^2$, formed by charge transfer in the H target (producing the same integral cross section) would be deflected to angles near $\pi - \theta$. The spin-exchange cross section thus tends to the charge transfer cross section in the CDP limit, while the elastic cross section in Eq. (7) leads to the “total” differential cross section. The energy at which this condition of distinguishability holds is well established (see, e.g., Ref. [16]) and we find that it occurs for $E > 1$ eV. At lower energies the interference between the elastic and charge transfer channels leads to deviation between the two definitions of the elastic cross section if this separation is performed.

The $1s\sigma_g$ and $2p\sigma_u$ adiabatic electronic quasimolecular curves of H_2^+ for a series of fixed separations R of the nuclei can be calculated with arbitrary accuracy owing to the fact that the one-electron, two-center problem is separable in prolate elliptic coordinates [17]. In the present work, we calculated the gerade and ungerade potentials and their derivatives with nine-digit accuracy at 10^5 points from $R = 0.0002$ to 50 a.u., thus reducing the error in interpolating the potentials at the points required by the numerical solver. For larger distances, we used the asymptotic expansion for the adiabatic potentials up to 11th order [18].

The radial equations were solved by the algorithm proposed by Johnson [19] for solution of the stationary Schrödinger equation using the logarithmic derivatives for each partial wave, with $R_{\text{max}} = 800$ and with $R_{\text{min}} = 0.01$ a.u.. The step ΔR in R used on the numerical mesh was 0.0001 a.u. for all energies. The convergence of the elastic S -matrix elements in partial waves was established for each energy by requiring that $\text{Re}\{1 - S_L\} \leq 10^{-8}$ for at least 20 consecutive partial waves [see Eq. (3)]. For example, the resulting value of L_{max} was 69 at 10 eV but reached 3200 for 10 eV. The numerical parameters used (i.e., the step and accuracy in calculations of the potential, ΔR and R_{max} in the solver as well as the number of partial waves L_{max}) have been adopted after a series of tests. Their further improvement introduces change in the eighth (at lower energies) and seventh (at higher energies) significant digit in the cross sections for elastic scattering and spin exchange in $\text{H}^+ + \text{H}$ collisions, providing an overall accuracy to at least six significant digits.

The cross sections have been computed for as many points per energy decade as needed, depending on the oscillating features of the cross sections and anticipated resonances. Such a requirement led to 664 energies for the energy range considered. The calculation was performed using a 2-GHz Xeon-CPU-based work station. The CPU time was mostly influenced by the number of partial waves required, varying from on the order of 10 min (for the lowest energies) to on the order of a day (for the highest energies) per energy point.

It is important to note that the reported accuracy to six significant digits is the numerical accuracy, obtained by careful control of the numerical parameters of the problem. The physical accuracy, on the other hand, depends on the level of physical phenomena included in the numerical model. For example, to test the physical accuracy of our approach at energies above the threshold for inelastic processes (about

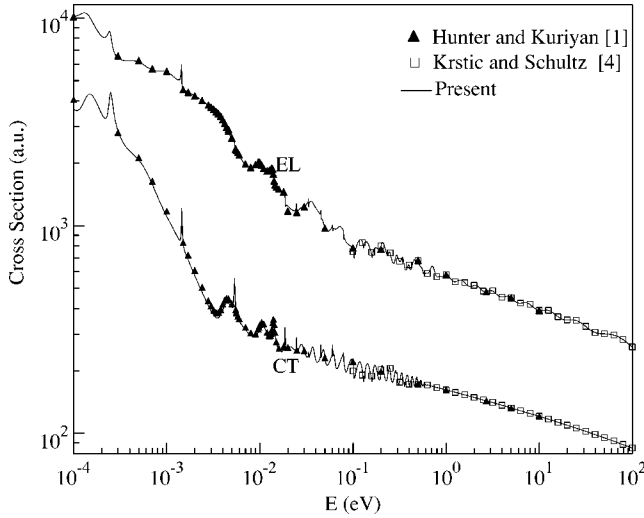


FIG. 1. Elastic (EL) and spin-exchange (CT) cross sections as a function of center-of-mass collision energy, calculated as described in Sec. II A.

10 eV) we included the rotational coupling with a third state, $2p\pi$, in the model, which is the first candidate to contribute to the inelastic charge transfer to $H(n=2)$. As a result, the charge transfer and elastic cross sections changed in the third digit at 100 eV. The details of this calculation were presented in Ref. [4]. The estimate of relativistic and nonadiabatic corrections, which are not included in the model and that can play a role at the low-energy end of the range considered (10^{-4} eV and lower) is planned for the future work.

Figure 1 shows the present elastic (EL) and charge transfer (CT, spin exchange) cross sections for all five decades of the energy range considered. Comparison was made with the early calculations of Hunter and Kuriyan [2] (HK) for energies 10^{-4} –10 eV, and recent calculations of Krstić and Schultz [4] for 0.1–100 eV. The latter calculation was done with somewhat lesser numerical requirements, on a coarse energy grid and does not show any deviation visible in the figure from the present values. The HK calculation picked up some of the structures of the cross section, and their deviation, reaching up to a few percent from the present values, can be ascribed to a much coarser potential grid (67 values for $R \leq 50$ a.u.), as well as to a significantly coarser numerical grid and a smaller number of partial waves in calculation of the cross sections. Hodges and Breig [3] (HB) (not shown in the figure) performed detailed calculations in the same energy range as Hunter and Kuriyan, reproducing most of the resonant structures in Fig. 1, but using the same coarse potential grid employed by Hunter and Kuriyan. We discuss the present results in more detail in Sec II C.

B. Resonances and S -matrix poles

In the present case the poles of the S matrix correspond to resonances associated with potential barriers formed by the attractive polarization and exchange potentials and the repulsive centrifugal potentials. In the WKB approximation the S matrix has no poles [20], therefore we use the comparison equation technique [21] to calculate the poles of the S matrix.

According to this approach [10] the phase shift η_l has the form

$$\eta_L = \eta_L^{\text{WKB}} + 2\phi_0 + \arctan \left[\frac{1-A}{1+A} \tan(\phi_2 + \phi_0) \right], \quad (13)$$

where we define

$$\phi_2 = \int_{R_0}^{R_1} \sqrt{q(R')} dR', \quad (14)$$

$$q(R) = 2\mu[E - V_{\text{eff}}(R)], \quad (15)$$

$$V_{\text{eff}}(R) = V(R) + \frac{(L+1/2)^2}{2\mu R^2}, \quad (16)$$

$$\phi_0 = \frac{1}{2} \arg \Gamma\left(\frac{1}{2} + ia\right) + \frac{a}{2}(1 - \ln\langle a \rangle), \quad (17)$$

and

$$A = 1/\sqrt{1 + e^{-2\pi a}}, \quad (18)$$

$$a = \frac{1}{\pi} \int_{R_1}^{R_2} \sqrt{-q(R')} dR', \quad (19)$$

and R_i are turning points determined by $q(R_i)=0$ where $i=0, 1, 2$. If we further define R_T as the position of the top of barrier where $V_{\text{eff}}(R)$ has a maximum than we see that for $E > V_{\text{eff}}(R_T)$, $R_1=R_2$ are the complex zeros of $q(R)$. A similar expression for the phase shift was given in Ref. [20] but the approximations used for $\arg \Gamma(\frac{1}{2} + ia)$ precluded calculations of the poles of the S matrix. Using the definition of the S matrix, $S = \exp(i2\eta_L)$ and phase shift from Eq. (13) we obtain the expression for the S matrix

$$S_L = S_L^{\text{WKB}} e^{4i\phi_0} \frac{1 + Ae^{-2i\phi_2 - 2i\phi_0}}{1 + Ae^{2i\phi_2 + 2i\phi_0}}. \quad (20)$$

From Eq. (20) we see that the S matrix has poles at complex values of E when the denominator in Eq. (20) becomes zero. It can be easily shown that the equation defining the poles of the S matrix has the form

$$\phi_2 + \phi_0 + \frac{i}{4} \ln(1 + e^{-2\pi a}) = \pi \left(n + \frac{1}{2} \right). \quad (21)$$

To find roots of the Eq. (21) in the complex E plane we use the analytic continuation of $\arg \Gamma(\frac{1}{2} + iz)$ to the complex plane,

$$\arg \Gamma\left(\frac{1}{2} + iz\right) = -\frac{i}{2} \ln \frac{\Gamma\left(\frac{1}{2} + iz\right)}{\Gamma\left(\frac{1}{2} - iz\right)}.$$

The positions of the poles of the S matrix in the complex E plane corresponding to various types of resonances are

TABLE I. Below-barrier resonances.

l	Re E (eV)	Im E (eV)	l	Re E (eV)	Im E (eV)
4	0.000226	0.000012	25	0.080	0.00026
7	0.00145	0.000016	26	0.0713	6.7×10^{-7}
10	0.00536	0.000072	27	0.103	0.0061
12	0.00549	3.0×10^{-7}	28	0.097	5.3×10^{-7}
13	0.0144	2.4×10^{-6}	29	0.131	0.012
14	0.0059	2.0×10^{-9}	30	0.127	0.000033
15	0.0188	0.00018	31	0.118	8.1×10^{-8}
16	0.0081	1.9×10^{-7}	32	0.162	0.00015
17	0.0249	0.000073	33	0.156	1.0×10^{-6}
18	0.0130	2.0×10^{-10}	34	0.202	0.00051
19	0.0336	0.000051	35	0.199	7.8×10^{-6}
20	0.0214	9.0×10^{-10}	36	0.247	0.0012
21	0.0454	0.000063	37	0.248	0.000036
22	0.0337	7.5×10^{-9}	38	0.244	1.8×10^{-7}
23	0.0608	0.00012	39	0.303	0.000097
23	0.0146	1.0×10^{-14}	40	0.302	5.0×10^{-7}
24	0.0503	7.2×10^{-8}	41	0.364	0.00013

tabulated in Tables I–IV. Namely, we find three types of resonances, below-barrier resonances (Table I), top-of-barrier resonances (Table II), and above-barrier resonances (Table III). For a chosen L we assign to the top-of-barrier resonance that pole whose real part of energy, $\text{Re}\{E_p\}=E_B$, is closest to top of the barrier, $V_B(L)$. Then the poles with $\text{Re}\{E_p\}<E_B$ are assigned the names “below-barrier” and

those with $\text{Re}\{E_p\}>E_B$ the “above-barrier” resonances. In case of the below-barrier resonances the particles are confined by the potential barrier in a region $R_0<R<R_1$. In the limit $\hbar\rightarrow 0$ the width vanishes exponentially and the motion is described by classical bound state trajectories. The top-of-barrier resonances are orbiting resonances and their widths are proportional to \hbar . In the classical limit these resonances

TABLE II. Top-of-barrier resonances ($1s\sigma$).

l	Re E (eV)	Im E (eV)	l	Re E (eV)	Im E (eV)
3	0.000218	0.00015	23	0.0792	0.0096
4	0.00638	0.00060	24	0.0815	0.0032
5	0.00101	0.00028	25	0.0996	0.012
6	0.00210	0.00098	26	0.103	0.0044
7	0.00389	0.0024	27	0.124	0.015
8	0.00414	0.00061	28	0.128	0.0062
9	0.00673	0.0019	29	0.152	0.018
10	0.00997	0.0043	30	0.157	0.0088
11	0.0103	0.0012	31	0.162	0.0025
12	0.0143	0.0036	32	0.191	0.0012
13	0.0202	0.0076	33	0.198	0.0042
14	0.0207	0.0029	34	0.231	0.016
15	0.0276	0.0073	35	0.240	0.0065
16	0.0282	0.0024	36	0.276	0.020
17	0.0369	0.0073	37	0.287	0.0092
18	0.0375	0.0021	38	0.275	0.0014
19	0.0483	0.0075	39	0.341	0.012
20	0.0492	0.0022	40	0.355	0.0030
21	0.0623	0.0083	41	0.401	0.013
22	0.0638	0.0025	42	0.420	0.0027

TABLE III. Above-barrier resonances ($1s\sigma$).

l	Re E (eV)	Im E (eV)	l	Re E (eV)	Im E (eV)
21	0.112	0.095	32	0.260	0.10
22	0.108	0.067	33	0.235	0.0042
23	0.132	0.095	34	0.293	0.095
24	0.125	0.064	35	0.292	0.0065
25	0.160	0.11	36	0.343	0.11
26	0.152	0.072	37	0.343	0.0073
27	0.192	0.12	38	0.342	0.0041
28	0.184	0.081	39	0.413	0.10
29	0.219	0.12	40	0.399	0.045
30	0.229	0.11	41	0.498	0.16
31	0.196	0.0034	42	0.499	0.12

are related to the motion of the particles along periodic unstable trajectories with $R(t)=R_T$. The width of the above-barrier resonances does not go to 0 as $\hbar \rightarrow 0$ and these states have no classical analog.

A few poles of the S matrix for scattering on the $2p\sigma$ -ungerade potential are assigned to the top-of-barrier resonances. These are shown in Table IV.

C. Analysis

In the previous section we have correlated some structure with the poles of the S matrix. In the case of narrow resonances with near Lorentzian line shapes the correspondence is good. In all cases it proves useful to examine individual partial waves to check the fit to the Fano line-shape formula

$$\sin^2 \eta = \sin^2 \eta_0 \frac{(q + \varepsilon)^2}{1 + \varepsilon^2}, \quad (22)$$

where the line-shape parameters are defined as $q = \cot \eta_0$ and $\varepsilon = 2(E_r - E)/\Gamma$. It is assumed that E_r , Γ , and η_0 are slowly varying functions of E . Furthermore, in the present analysis we assume that E_r and $\Gamma/2$ are constants given by real and imaginary parts of the positions of the poles, E_p , but recognize that this approximation is often not applicable.

Figure 2 shows details of resonances found in the first two decades (10^{-4} – 10^{-2} eV) of Fig. 1. The values of the orbital angular momentum L for various resonant structures in Fig. 2 corresponding to the poles of the S matrix in Tables I–IV are shown, together with the type of the resonances [below-barrier (BB), top-of-barrier (TB), above-barrier (AB)]. The descriptor “u” in Fig. 2 is used for resonances of the $2p\sigma$ -ungerade potential. All other resonances are from the $1s\sigma$ -gerade potential, and these do not carry any descriptor on Fig. 2 and all subsequent figures.

TABLE IV. $2p\sigma$ top-of-barrier and above-barrier resonances.

l	Re E (eV)	Im E (eV)	Re E (eV)	Im E (eV)
3	0.000148	0.000039	0.000282	0.00031
4	0.000497	0.00017	0.000727	0.00081

Figure 3 shows the computed and fitted $\sin^2 \eta_g$ near a below-barrier (BB) resonance at $E_r = 1.45 \times 10^{-3}$ eV with a width $\Gamma = 3.2 \times 10^{-5}$ eV for $L=7$ (see Table I). With a value of $\eta_0 = 0.4$ the computed and fitted profiles agree very well. In this case the resonance displays a typical Fano profile associated with a stable classical orbit.

In contrast Fig. 4 shows the fit to a top-of-barrier resonance of u symmetry for $L=3$. In this case we know that there are no stable classical orbits so the resonance is relatively broad, $\Gamma \approx E_r/2$ (Table IV). The corresponding fit to the Fano profile has $\eta_0 = 0.1$. It is apparent that the position of the peak agrees well the real part of E_p , i.e., E_r , however, the apparent width is much greater than $2 \text{Im}\{E_p\} = \Gamma$ and the shapes do not agree. The agreement in position supports our interpretation of this structure as an above the barrier resonance, however, the approximations that η_0 and Γ in the Fano line-shape formula are constant is questionable. The quantity E_p computed in the previous section is defined to be a constant, however, the relationship of this quantity to the phase shift usually involves dynamical factors, i.e., functions of E that are unknown. For this reason, the correlation of

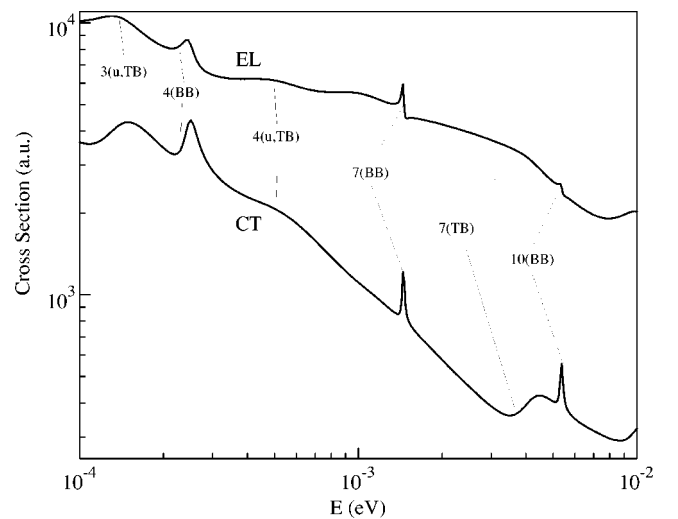


FIG. 2. Assignment of the resonances in Tables I–IV to the structures in Fig. 1.

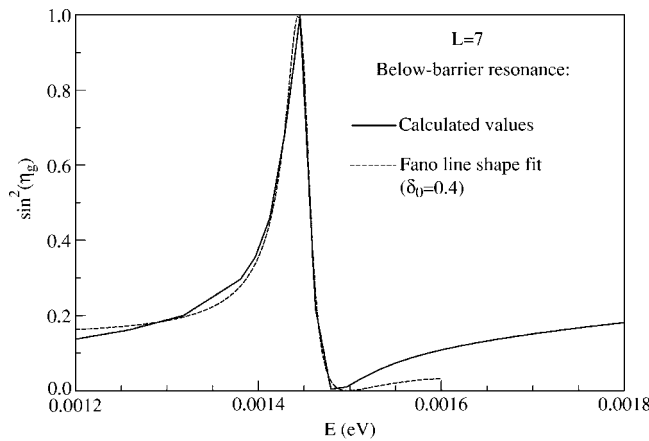


FIG. 3. Below-barrier (BB) shape resonance in the gerade ($1s\sigma_g$) potential for $L=7$ (see Table I). The fit was made to the Fano line-shape formula of Eq. (22).

some of the resonance poles and the structures of the cross section using the resonance formula is only semiquantitative.

Figure 5 shows the assignments of the resonances from Tables I and II to the structures in the elastic and charge-transfer cross sections in the 10^{-2} – 10^{-1} -eV decade of collision energies. This region is rich in structures that emerge from the below-barrier and top-of-barrier resonances. Below-barrier resonances in Fig. 6 are mainly very narrow on the scale of the collision energies 0.1–2 eV, shown in this figure. We have been able to identify most of them with the widths that are at most four orders of magnitude smaller than the relevant energies. Still, the majority of the structures in this figure are caused by the top-of-barrier (TB) and above-barrier (AB) resonances, and we identify most of them.

Since the gerade phase shift η_g is a component that dominates the structure of the elastic cross section in Eq. (8) as well as of charge-transfer one in Eq. (11), we show in Fig. 7 both η_g and $\sin^2(\eta_g)$ for the partial wave $L=30$. All three types of resonances, BB, TB, and AB, are present. The TB and AB are here of the window type. The positions of the BB and TB exactly follow the values from the tables, while the AB case is shifted in position by about 0.01 eV (to 0.217

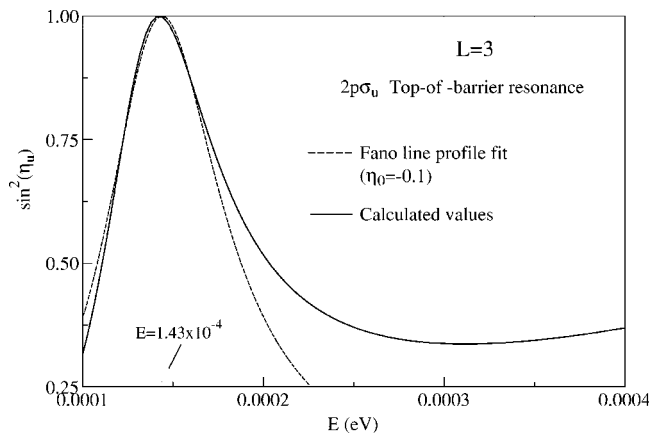


FIG. 4. Top-of-barrier resonance in the antibonding ($2p\sigma_u$) potential for $L=3$ (Table IV). The fit was made to the Fano line-shape formula of Eq. (22).

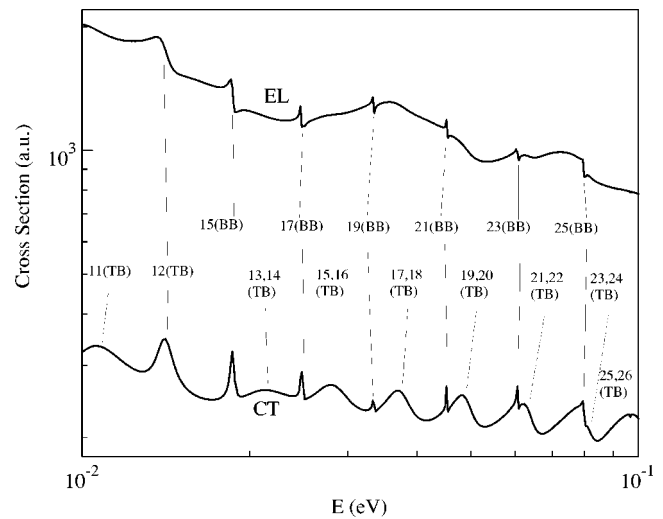


FIG. 5. Assignment of the resonances in Tables I–IV to the structures in Fig. 1.

from 0.229 eV). This is not a surprise having in mind that the width of the AB resonance for $L=30$ in Table III is about the same as its energy.

The narrow resonance structures discussed up to now have been at relatively low energies, below 0.1 eV, where they are fairly common. They occasionally do occur at much higher energies, according to Table I. This is illustrated in Fig. 8 which shows $\sin^2 \eta_g$ for $L=41$, between 0.35 and 0.42 eV. In this region there is a narrow resonance at 0.364 eV, which fits a Fano profile but with a phase $\eta_0 = -2\pi/15$. The position and width were taken from Table I. Again the fit confirms that this is a narrow Fano resonance.

A broad peak at 0.398 eV is also seen in Fig. 8. This is correlated with the top-of-barrier resonance at $E_r=0.401$ eV, but, just as for the top-of-barrier resonance in Fig. 4, the width does not correlate with the corresponding $\text{Im}\{E_p\}$. In contrast to the earlier example, the computed width is narrower than $\text{Im}\{E_p\}$. It is remarkable, however, that the position of the structure still correlates well with $\text{Re}\{E_p\}$.

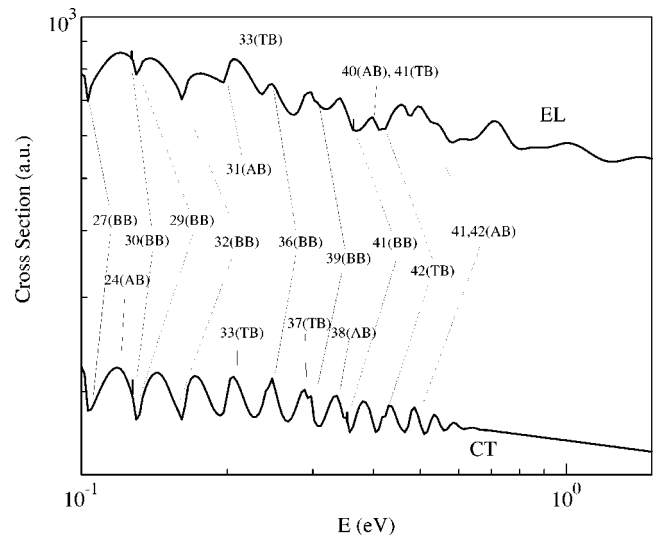


FIG. 6. Same as in Fig. 5.

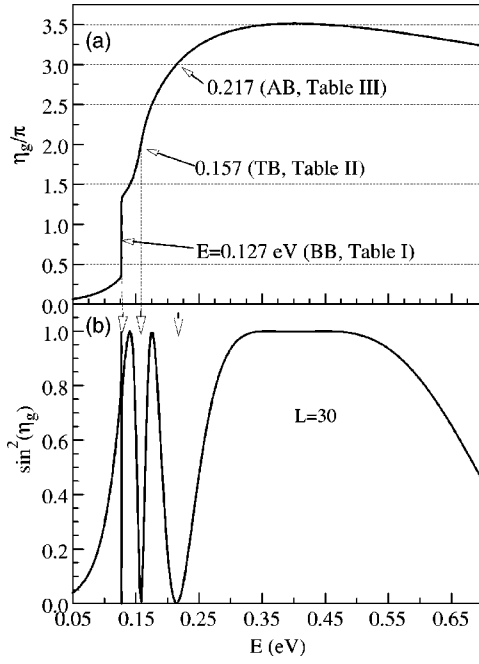


FIG. 7. Below-barrier (BB), top-of-barrier (TB), and above-barrier (AB) shape resonances of the window type in the gerade potential for $L=30$ (Tables I–III). The structures in (a) and (b) are discussed in the text.

The resonances identified in Sec. II B do not explain all of the features seen in the cross sections. Of particular interest are the oscillations in the higher energy region which occur in some cross sections but not in others. A long time ago Bernstein [22] pointed out that sums over partial elastic cross sections involving $\sin^2 \eta_L$ and constituting the integral cross section may oscillate for some types of the potential if η_L has a maxima or minima where $d\eta_L/dL$ vanishes. These are called glory oscillations in the integral elastic cross section. The contributions to the sum for regions where $d\eta_L/dL=0$ are estimated using the method of stationary phase [11,12]. The stationary phase contribution is found to be

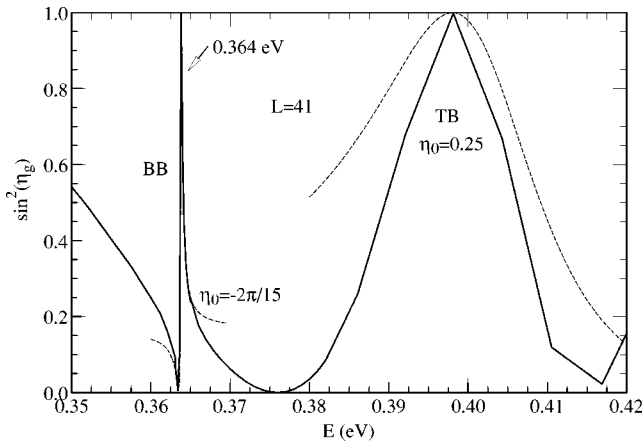


FIG. 8. The shape resonances for $L=41$. The sharp peak at $E=0.364$ eV is below-barrier (BB) resonance. The wider structure at $E=0.398$ eV is the top-of-barrier (TB) resonance (Table II).

$$\sigma_{\text{sp}} = -2\pi^{3/2}k^2(2L_0+1) \left| \frac{d^2\eta}{dL^2} \right|_{L=L_0}^{-1/2} \cos[2\eta(L_0) + \pi/4], \quad (23)$$

where L_0 is the orbital angular momentum corresponding to the stationary phase.

It is then supposed that the reduced cross section $\bar{\sigma} = \sigma - \sigma_{\text{sp}}$ is a smooth function of energy. This smooth function is sometimes evaluated by assuming an average value of $\sin^2 \eta_L = 1/2$ for values of L less than some maximum value L_{max} . This latter assumption is not necessary but it is necessary to assume that \bar{Q} is smooth. In that case the true cross section $\sigma = \bar{\sigma} + \sigma_{\text{sp}}$ will show oscillations with an amplitude and phase given by Eq. (23).

To put the formula above on a more firm foundation for the case of elastic scattering we evaluate the sum of $\sin^2 \eta_L$ over L by dividing the sum at $L=L_1$ where η_L is less than $\pi/2$ for $L > L_1$ and drops smoothly to zero with increasing L . Thus

$$\begin{aligned} Q &= \frac{4\pi}{k^2} \sum_{L=0}^{L_1} (2L+1) \left(\frac{1 - \cos(2\eta_L)}{2} \right) + \frac{4\pi}{k^2} \sum_{L=L_1}^{\infty} (2L+1) \sin^2 \eta_L \\ &= \bar{Q} - \frac{4\pi}{k^2} \sum_{L=0}^{L_1} (2L+1) \frac{\cos(2\eta_L)}{2}. \end{aligned} \quad (24)$$

Normally, the sum over $\cos(2\eta_L)$ is negligibly small due to cancellation of positive and negative terms, but if there are points of stationary phase the cancellation is incomplete and there will be some contribution from the second term in Eq. (24). This contribution is evaluated by the method of stationary phase to obtain Eq. (23) and an explicit expression for $\bar{\sigma}$, namely,

$$\bar{Q} = \frac{2\pi}{k^2} L_1(L_1+1) + \frac{4\pi}{k^2} \sum_{L=L_1}^{\infty} (2L+1) \sin^2 \eta_L, \quad (25)$$

where it is understood that L_1 is a function of E . In general the stationary phase evaluation will miss contributions owing to incomplete cancellation at the end point $L=L_1$. Because this is expected to vary slowly with energy we can assume that these slowly varying contributions are included in \bar{Q} . Orbital angular momentum where the stationary phase (SP) of $\eta(L)$ for scattering on the $1s\sigma_g$ potential is shown in Fig. 9(a), as well as the corresponding amplitudes of oscillations, defined in Eq. (23) in terms of the second derivatives, $d^2\eta/dL^2$, shown in Fig. 9(b). Since the stationary phase approximation, being an asymptotic method, is well defined only for large the second derivatives, the rising part of the amplitude in Fig. 9(a) above 10 eV of the collision energy is not expected to be correct [dashed-line rectangle in Fig. 9(a)], having in mind small values of $d^2\eta/dL^2$ for these energies. This also explains a small deviation of the SP oscillation amplitudes from the exact values at the higher energy end of Fig. 10. This figure shows our result for the oscillations in the elastic cross section, induced by the glory effect. It reproduce the oscillations (above about 1 eV) and modulate the cross section at lower energies, as shown in Fig. 10.

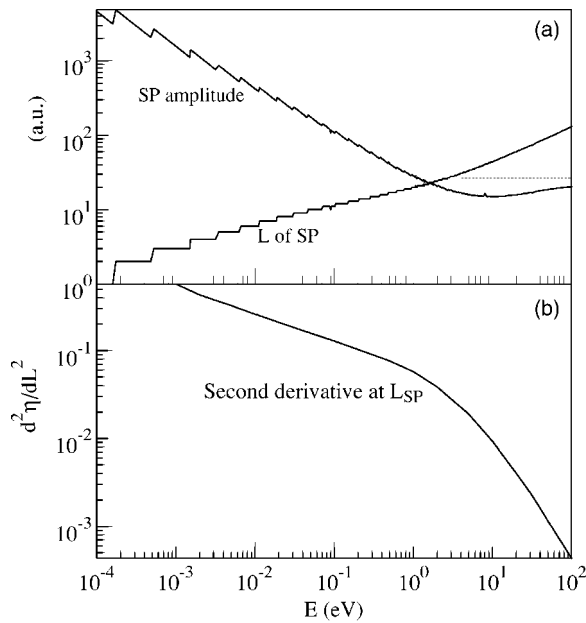


FIG. 9. (a) L and amplitude of Eq. (23) at stationary phases (SP) of $\eta_g(L)$, as a function of E ; (b) The second derivative of $\eta_g(L_{SP})$, used for computing of the SP amplitude in (a).

Agreement is achieved in the phase, frequency and amplitude, removing any doubt regarding the source of the oscillations. It is interesting to note that the ungerade phase shift, $\eta_u(L)$, also has a glory effect, i.e., stationary phase in L . But this appears for large L 's where $\eta_u(L)$ is so small that any oscillations disappear already at energies above 10^{-2} eV, as also shown in Fig. 10.

The absence of the stationary phase in the difference $\eta_g(L) - \eta_u(L)$ [see Eq. (11)] explains the absence of the glory oscillations in the charge-transfer cross section.

III. CONCLUSIONS

We have performed a highly accurate (to at least at six significant digits) calculation of the elastic and spin-exchange cross sections in collisions of protons with hydro-

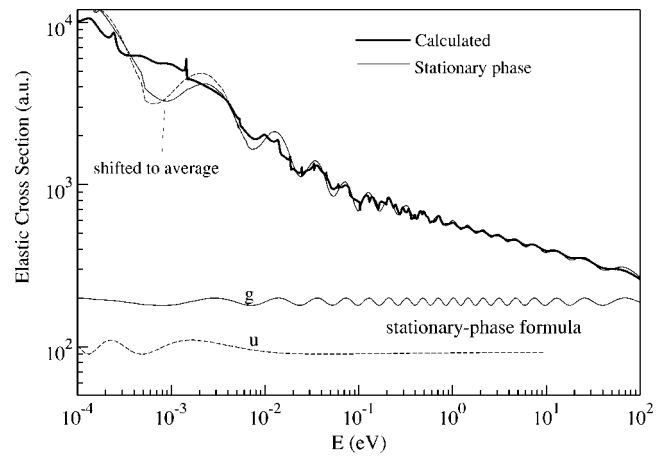


FIG. 10. Glory oscillations in the elastic cross section, reproduced by the stationary-phase formula of Eq. (23).

gen in the ground state. The calculation was performed covering the range of the center-of-mass energies 10^{-4} – 10^2 eV, on a dense mesh of the energy points (more than 800), to resolve all structures that appear in the cross sections, at both the lowest and highest energies of the considered energy range. Calculating the poles of the S matrix, we were able to tabulate and identify in the cross sections all narrow resonant structures, originating from the below-barrier, above-barrier, and sometimes from the top-of-barrier shape resonances. We also identify the wide structures at lower energies with often overlapping top-of-barrier and above-barrier shape resonances. The structures in the elastic cross section at energies below 1 eV are modulated by the stationary phase in the L dependence of the phase shift (glory effect). The oscillations continue into the energy range where the resonant structures are absent, appearing as the only structure in the cross section at higher energies (up to at least 100 eV).

ACKNOWLEDGMENTS

We acknowledge support from the U.S. Department of Energy, Offices of Basic Energy and Fusion Energy Sciences, through Oak Ridge National Laboratory, managed by UT-Battelle, LLC under Contract No. DE-AC05-00OR22725.

- [1] G. Hunter and M. Kuriyan, Proc. R. Soc. London, Ser. A **358**, 321 (1977).
- [2] G. Hunter and M. Kuriyan, Proc. R. Soc. London, Ser. A **353**, 575 (1977).
- [3] R. R. Hodges and E. L. Breig, J. Geophys. Res. **35**, 7697 (1991).
- [4] P. S. Krstić and D. R. Schultz, J. Phys. B **32**, 3485 (1999).
- [5] P. S. Krstić and D. R. Schultz, Phys. Rev. A **60**, 2118 (1999).
- [6] P. S. Krstić and D. R. Schultz, *Atomic and Plasma-Material Interaction Data for Fusion*, APID Series STI/PUB/023/APID/08 (IAEA, Vienna, 1998), Vol. 8, p. 1.
- [7] E. Vogt and G. H. Wannier, Phys. Rev. **95**, 1190 (1954).
- [8] U. Fano, Phys. Rev. **124**, 1866 (1961).
- [9] N. F. Mott and H. S. W. Massey, *The Theory of Atomic Collisions*, Third Edition (Clarendon Press, Oxford, 1965), p. 359.
- [10] J. H. Macek and S. Yu. Ovchinnikov, Phys. Rev. A **50**, 468 (1994).
- [11] M. S. Child, *Semiclassical Mechanics with Molecular Applications* (Clarendon Press, Oxford, 1991).
- [12] E. E. Nikitin and S. Ya. Umanskii, *Theory of Slow Atomic Collisions* (Springer-Verlag, New York, 1984).
- [13] G. Hunter and M. Kuriyan, At. Data Nucl. Data Tables **25**, 287 (1980).
- [14] B. H. Bransden and M. R. C. McDowell, *Charge Exchange and the Theory of Ion-Atom Collisions* (Clarendon Press, Oxford, 1992).

- [15] F. Masnou-Seeuvs and A. Salin, J. Phys. B **2**, 1274 (1969).
- [16] F. J. Smith, Proc. Phys. Soc. London **92**, 866 (1966); Planet. Space Sci. **14**, 929 (1966).
- [17] M. Abramowitz and I. A. Stegun, *Handbook of Mathematical Functions* (Dover, New York, 1972).
- [18] R. J. Damburg and R. Kh. Propin, J. Phys. B **1**, 681 (1968).
- [19] B. Johnson, J. Comput. Phys. **13**, 445 (1973).
- [20] K. W. Ford, D. L. Hill, M. Wakano, and J. H. Wheeler, Ann. Phys. (N.Y.) **7**, 239 (1959).
- [21] D. I. Abramov, S. Yu. Ovchinnikov, and E. A. Solov'ev, Phys. Rev. A **42**, 6366 (1990).
- [22] R. B. Bernstein, Adv. Chem. Phys. **10**, 75 (1966).